

## Interfacial and Bulk Nanostructure of Liquid Polymer Nanocomposites

Samila McDonald,<sup>†</sup> Jared A. Wood,<sup>‡</sup> Paul A. FitzGerald,<sup>‡</sup> Vincent S. J. Craig,<sup>§</sup> Gregory G. Warr,<sup>‡</sup> and Rob Atkin\*,<sup>†</sup>

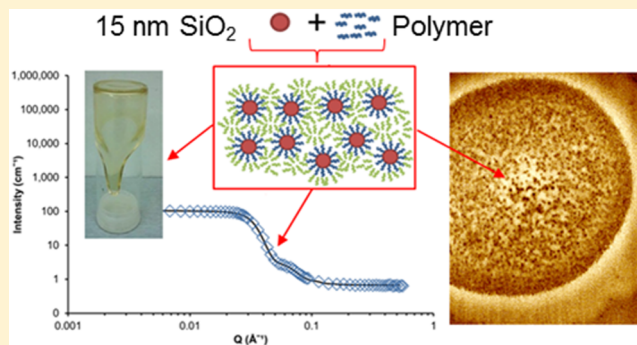
<sup>†</sup>The University of Newcastle, Newcastle, New South Wales 2308, Australia

<sup>‡</sup>The University of Sydney, Sydney, New South Wales 2006, Australia

<sup>§</sup>Australian National University, Canberra, Australian Capital Territory 0200, Australia

### Supporting Information

**ABSTRACT:** Liquid polymer nanocomposites (*l*-PNCs) have been prepared using silica nanoparticles with diameters of 15 nm (*l*-PNC-15) and 24 nm (*l*-PNC-24), and Jeffamine M-2070, an amine-terminated ethylene oxide/propylene oxide (PEO/PPO, ratio 31/10) copolymer. Jeffamine M-2070 was used as the host liquid in which the particles were suspended and was also grafted onto the particle surface to prevent aggregation. The grafting density of Jeffamine M-2070 on the particle surfaces was  $\sim 0.75$  chains  $\text{nm}^{-2}$ . When the total polymer content (surface layer + host) was greater than  $\sim 30$  wt %, the PNC was a liquid, while at lower polymer volume fractions the PNC was solid. In this work, the bulk and surface structures of *l*-PNCs with  $\sim 70$  wt % polymer and 30% silica are characterized and compared. Small-angle neutron scattering (SANS) was used to probe the bulk structure of the *l*-PNCs and revealed that the particles are well-dispersed with minor clustering in *l*-PNC-15 and substantial clustering in *l*-PNC-24. This is attributed to stronger van der Waals attractions between particles due to the larger particle size in *l*-PNC-24. Corresponding effects were revealed using tapping mode atomic force microscopy (TM-AFM) at the *l*-PNC–air interface; clustering was minimal on the surface of *l*-PNC-15 but significant for *l*-PNC-24 droplets. In regions of the *l*-PNC where the particles were well-dispersed, the spacing between particles is consistent with their volume fractions. This is the first time that the distribution of polymer and particles within *l*-PNCs has been imaged *in situ*.



## INTRODUCTION

In a polymer nanocomposite (PNC), nanoparticles (filler) are dispersed in a polymer matrix to produce a new hybrid material incorporating the useful properties of both components.<sup>1</sup> A PNC may be a solid (*s*-PNC), liquid (*l*-PNC), or gel, depending on the properties and volume fractions of the filler and host polymer.<sup>2,3</sup> Addition of the filler can enhance the thermal stability, mechanical strength, and optical properties of the host polymer, while the host polymer improves the processability of the filler material.<sup>4–6</sup> The PNC host polymer may be a homopolymer, block copolymer, random copolymer, polyelectrolyte, or a polymer blend, while the nanosized filler can be spherical, rod-like, or sheet-like in form.<sup>4,7</sup> Metal oxide nanoparticles (silica,<sup>8,9</sup> titania,<sup>10,11</sup> and polyoligosilsesquioxane (POSS)<sup>12</sup>), metal nanoparticles (gold<sup>4,13</sup> and platinum<sup>13</sup>), quantum dots (CdSe nanocrystals<sup>4</sup>), layered sheets (silicate<sup>14</sup>), and carbon-based nano-objects (spherical buckminsterfullerene,<sup>2</sup> carbon nanotubes,<sup>15</sup> and functionalized graphene sheets<sup>16,17</sup>) have all been used as nanofillers, among many others. Spherical silica nanoparticles are one of the most

popular fillers because of their useful properties and ease of synthesis.<sup>18</sup>

A key challenge for the preparation of PNCs, especially at appreciable inorganic loadings, is the tendency of the nanomaterial to aggregate.<sup>6,18</sup> Particle aggregation in PNCs is a consequence of the thermodynamic requirement to reduce the interfacial area between the filler and the polymer due to their enthalpic incompatibility, the reduction in entropy that occurs when polymers are confined between particles, and van der Waals attractions between particles.<sup>6</sup> To prevent aggregation, nanoparticles are often modified by grafting short polymers to the particle surface.<sup>4,19,20</sup> This leads to steric repulsions between the nanoparticles and improves the compatibility between the filler and the host polymer.<sup>4,9</sup> Polymers are attached to the particle surface by either the “grafting from” method, where ligands or initiators are covalently grafted onto nanoparticles and the grafted polymer

Received: January 22, 2015

Revised: March 3, 2015

Published: March 4, 2015



is synthesized *in situ*, or the “grafting to” method, where end-functionalized polymers are covalently grafted onto nanoparticles directly. The “grafting to” method is simpler, but lower grafting densities can mean that particle aggregation still occurs.<sup>21</sup> The more synthetically complicated “grafting from” method can enable higher and better defined grafting densities, and the degree of polymerization can be controlled.<sup>9</sup>

The physical properties of a PNC can be coarsely controlled via selection of the polymer and particle type, with more subtle tuning possible through varying the host polymer length, particle size, particle volume fraction, and length and grafting density of the polymer attached to the particle surface.<sup>4,5,9</sup> Phase diagrams revealing the effect of these parameters have been reported.<sup>3</sup> The electrical properties, optical properties, high thermal stability, hardness, and modulus of *s*-PNCs have seen them used for protective coatings,<sup>8</sup> photocatalysis,<sup>4,8</sup> biosensors,<sup>8</sup> organic light-emitting devices (OLEDs),<sup>2,4</sup> and solar cells,<sup>4,22</sup> among other applications. *l*-PNCs are of interest because of their potential as lubricants,<sup>23</sup> electrolytes,<sup>24–26</sup> and carbon capture solvents,<sup>27–31</sup> as well as their capacity to modify interfacial properties. For *l*-PNCs, the particle size, volume fraction, and type and length of both the grafted and host polymers control viscoelasticity.<sup>32–34</sup> The ratio of the grafted and host polymer molecular weights determines whether the grafted polymer is “wetted” or “dewetted”. When the grafted polymer is dewetted, phase separation occurs. Therefore, *l*-PNCs need to be carefully designed to produce well-dispersed grafted nanoparticles that are wetted by the host polymer and remain liquid at high particle loading.

A subset of *l*-PNCs, known as nanoparticle organic hybrid materials (NOHMs), are liquid without added host polymer, i.e., the ionically (*I*-NOHMs) or covalently (*C*-NOHMs) surface-grafted polymer serves as the “solvent”.<sup>9,10,19,25,27–31,35–42</sup> Polymer dynamics of *I*-NOHMs have been studied using NMR.<sup>36,40</sup> It was found that there is a strongly associated polymer layer with a slow diffusion rate closest to the particle surface and a weakly associated polymer layer with a faster diffusion rate farther from the particle surface. The weakly associated polymer layer is able to exchange between nearby particles, which imparts fluidity to the system. In this way, the grafted polymer “self-suspends” the nanoparticles. However, for *C*-NOHMs, the covalently grafted polymer cannot exchange between particles; to completely fill the interstitial volume, the grafted chains must stretch. It is somewhat unclear whether *C*-NOHMs are truly liquid without a dispersing polymer,<sup>27,28</sup> as conventional polymer-grafted nanoparticles are typically solids at the same particle concentration.<sup>3,6,43</sup>

Although several studies have reported the bulk structure of *l*-PNCs, more specifically NOHMs,<sup>9,19,36,40,41,44</sup> the surface structure is unexplored. In this study *l*-PNCs are prepared using two different sized silica particles (15 and 24 nm), and an amine-terminated PEO/PPO copolymer (Jeffamine M-2070, PEO/PPO ratio 31/10) is used as both the host and grafted polymer. For both samples, the particle concentration was ~30 wt %. Small-angle neutron scattering (SANS) is used to elucidate the bulk structure of *l*-PNCs while tapping mode atomic force microscopy (TM-AFM) reveals the structure of the interface between the *l*-PNCs and air. Together, these experiments reveal the structure of the *l*-PNCs in the bulk and at the air–liquid interface.

## EXPERIMENTAL SECTION

**Synthesis.** A 3 wt % silica stock solution was prepared by diluting 1.0 g of the silica suspension (2.5 g of LUDOX HS-40, 12 nm nominal particle size or 2.0 g of LUDOX TM-50, 22 nm nominal particle size) with ~30 g of Milli-Q water. The silica solution was then passed through an ion-exchange resin (DOWEX HCR-W2, Sigma-Aldrich) using a sintered funnel until the pH was ~2.5. A 3 wt % Jeffamine M-2070 (molecular weight (MW) = 2000 g/mol, PEO/PPO ratio = 31:10, Huntsman Chemicals) solution was prepared by diluting 3.0 g of Jeffamine M-2070 with 100 g of distilled ethanol. The solutions were sonicated for at least 5 min. The Jeffamine M-2070 solution was heated at 50 °C while stirring. (3-Glycidyloxypropyl)trimethoxysilane was added dropwise in a 1:1 stoichiometric ratio to the Jeffamine M-2070 solution. The polymer reaction solution was stirred at 50 °C for about 17 h in an unsealed conical flask. The 3 wt % silica solution (pH ≈ 2.5) was placed in a round-bottomed flask that was immersed in a 90 °C oil bath. The polymer solution was slowly added to the silica solution with vigorous stirring. The reaction solution was removed from the oil bath several times during the reaction and sonicated for 5 min to achieve a uniform product. After all of the polymer solution was added, the *l*-PNC reaction solution was left stirring at 90 °C for a further 3 h. Note that the polymer is heated above its lower critical solution temperature (LCST) (52 °C) and dehydration temperature (80 °C) during synthesis.<sup>45</sup> After the first several drops enter the silica solution, the solution goes cloudy and then returns to the same color as the stock silica solution after vigorous stirring and sonicating, meaning that any precipitates have redispersed into solution.

The *l*-PNC reaction solution was transferred into dialysis tubing (ThermoScientific Snakeskin 3500 MWCO, 22 mm diameter) ~30 cm in length. The solution was dialyzed for 24 h against Milli-Q water (volume ≈ 1.8 L). After dialysis, the *l*-PNC solution was transferred into a large beaker and dried at 60 °C. The resulting *l*-PNC is a transparent, pale yellow, viscous liquid. The water content of the *l*-PNCs was determined using Karl Fischer titration and was <2 wt % for all samples.

Some samples underwent an additional ultracentrifugation purification step to ensure removal of host polymer and produce a sample that consisted of only the silica particles and bound polymer. A known amount of *l*-PNC (<0.5 g) was dissolved in ~5 mL of Milli-Q water and then transferred into a plastic centrifuge tube (Quick-Seal, polypropylene tube, Beckman Coulter). The *l*-PNC solution was rinsed with Milli-Q water until the tube was filled. The tubes were sealed and placed in a fixed-angle rotor in a Beckman Coulter Optima L-100 XP Ultracentrifuge. The *l*-PNCs were centrifuged at 70 000 rpm for 40 min. The liquid supernatant was extracted from the plastic tubes, and the residue was dried using a rotatory evaporator (rotovap) at 5 mbar and room temperature to produce a white powder. This powder is denoted *s*-PNC.

**Thermogravimetric Analysis.** A PerkinElmer thermogravimetric analysis (TGA)/differential thermal analysis (DTA) instrument was used to determine the silica content and organic polymer content (in wt %) of *l*-PNCs and *s*-PNCs. Aluminum pans were used under a nitrogen atmosphere at a flow rate of 20 mL/min. The temperature was held at 30 °C for 1 min and then ramped from 30 to 550 °C at a rate of 10 °C/min.

**Dynamic Light Scattering.** A Malvern Zetasizer dynamic light scattering (DLS) instrument was used to measure the particle size of bare silica and *l*-PNCs, as well as the hydrodynamic diameter of free Jeffamine M-2070 polymer in aqueous solution, all at 25 °C. A 0.1 wt % particle suspension or polymer solution in distilled water was sonicated for at least 30 min prior to measurement. The size reported is the average of at least five measurements.

**Small-Angle X-ray Scattering.** Small-angle X-ray scattering (SAXS) was used to measure the particle size of bare silica particles at a dilution of 10 wt %. An Anton Paar SAXS instrument was used with a point source and 2–3 min exposure time.

**Small-Angle Neutron Scattering.** Small-angle neutron scattering (SANS) experiments were performed on hydrogenous *l*-PNC samples at the QUOKKA beamline at the Bragg Institute (ANSTO,

Australia) using 1 mm demountable cells. The neutron wavelength was 5 Å, and the temperature was set to 25 °C. Neutron scattering was collected at detector-to-sample distances of 1.3, 8, and 20 m for 300, 600, and 900 s, respectively, to achieve a  $q$  range from 0.003 to 0.6 Å<sup>-1</sup>. The scattering contrast in these experiments is derived from the difference between the neutron scattering length densities of silica ( $\sim 3.5 \times 10^{-6}$  Å<sup>-2</sup>) and Jeffamine M-2070 ( $\sim 0.68 \times 10^{-6}$  Å<sup>-2</sup>). In separate experiments, 10 wt % suspensions of *s*-PNCs were prepared in various H<sub>2</sub>O/D<sub>2</sub>O mixtures to give solvent scattering length densities of 3.0, 4.0, and  $5.0 \times 10^{-6}$  Å<sup>-2</sup>. The scattering patterns were analyzed using SASView software version 3.0.0 (www.sasview.org) and SASfit.

**Atomic Force Microscopy.** *l*-PNCs were prepared for atomic force microscopy (AFM) by dissolving a 0.01 wt % solution in ethanol and placing a single drop onto a freshly cleaved mica surface. Evaporation of the ethanol produced small droplets on the mica surface suitable for TM-AFM investigation, as reported previously.<sup>46</sup> A Nanoscope VIII AFM with silicon nitride tips was used to acquire both tapping mode images and contact mode force curves. The tips (model NSC36, Mikromasch, Tallinn, Estonia) had a nominal radius of 20 nm. The resonant frequency and spring constant were calibrated before beginning the experiment and ranged 200–220 kHz and 4.0–7.5 N m<sup>-1</sup>, respectively. The forces are normalized according to the tip radius (nominal 20 nm) and deflection sensitivity (measured during each experiment, typically 50 nm/V) according to standard methods.<sup>47</sup> Experiments were completed in a sealed AFM cell to minimize water ingress.

## RESULTS AND DISCUSSION

**Synthesis and Characterization of Liquid Polymer Nanocomposites.** *l*-PNCs were synthesized by grafting the amine-terminated PEO/PPO copolymer Jeffamine M-2070 onto silica.<sup>26–28</sup> The Jeffamine is reacted with a silane molecule (see Experimental Section), which then forms a covalent bond with the particle surface. Samples were prepared using two silica particle sizes with experimentally determined diameters of 15 and 24 nm. The *l*-PNCs produced using these particles are henceforth denoted *l*-PNC-15 and *l*-PNC-24.

The synthetic method used to prepare these *l*-PNCs has previously been reported to produce C-NOHMs.<sup>26–28</sup> For both *l*-PNC-15 and *l*-PNC-24, the product after dialysis and drying is also a viscous, pale yellow liquid. TGA of the *l*-PNCs revealed that the polymer is removed in a single step (Figure S1 in Supporting Information) upon heating and that *l*-PNC-15 was 71 wt % polymer and 29% silica, while *l*-PNC-24 was 69 wt % polymer and 31% silica. Both the description of *l*-PNCs and the TGA data is entirely consistent with previous reports of C-NOHMs.<sup>27</sup> However, ultracentrifugation of the dialysis product yielded white solids (*s*-PNCs) with much lower polymer contents of 23–27 wt %. This solid was readily redispersed into Jeffamine M-2070, yielding a waxy solid when the silica mass fraction was more than ~30% and a viscous liquid at all compositions below ~30 wt % silica. This confirms that the dialyzed product is a *l*-PNC, not a C-NOHM, and contains substantial amounts of free or host polymer (i.e., Jeffamine M-2070 that is not grafted to the surface). It is the free, ungrafted polymer that acts as the solvent and stabilizes the grafted particles, forming a fluid material. As such, the previous C-NOHM classification is incorrect for these systems.

TGA showed that, after ultracentrifugation, the polymer contents of *s*-PNC-15 and *s*-PNC-24 were 27 and 23 wt % polymer, respectively (Figure S2 in Supporting Information). This equates to grafting densities of 0.7 chains nm<sup>-2</sup> for *s*-PNC-15 and 0.8 chains nm<sup>-2</sup> for *s*-PNC-24, which is consistent with the reported grafting density of silane molecules onto silica nanoparticles (0.6 silane molecules nm<sup>-2</sup>).<sup>48</sup> That is,

Jeffamine M-2070 chain reacts with almost every available silane molecule present on the surface. Various reaction conditions were examined to ensure that maximum grafting density had been achieved, as a higher grafting density could potentially liquefy the *s*-PNCs into C-NOHMs.<sup>31</sup> When the synthesis was carried out at high pH, the solution after polymer addition was more viscous due to ungrafted silane cross-linking<sup>48,49</sup> and required ultracentrifugation at a higher rpm and longer time (80 000 rpm for 90 min) to purify. However, the appearance and composition (grafting density) of the sample after ultracentrifugation were otherwise unaffected. This insensitivity to pH suggests that commercial silica nanoparticle suspensions could be used without purification or modification for the synthesis of *l*-PNCs.

The structure of the unreacted silica nanoparticles (LUDOX HS and LUDOX TM) and individual polymer-coated nanoparticles was determined using transmission electron microscopy (TEM), dynamic light scattering (DLS), and small-angle X-ray and neutron scattering (SAXS and SANS). The particle sizes determined are shown in Table 1 and compared to

**Table 1. LUDOX Silica Particle Diameters in Dilute Aqueous Suspension before (LUDOX HS and LUDOX TM) and after Jeffamine M-2070 Is Grafted to the Surface (*l*-PNC-15 and *l*-PNC-24); DLS Reports Overall Hydrodynamic Diameter, whereas TEM, SAXS, and SANS Results Refer to the Silica Particle Diameter, Whether Coated or Not**

particle type	particle size (nm)				
	literature <sup>50</sup>	DLS	TEM	SAXS	SANS
LUDOX HS	12.1–16.3	15 ± 2	16 ± 2	16 ± 3	
<i>l</i> -PNC-15		35 ± 5	16 ± 1		16.4
LUDOX TM	25.3–28.1	24 ± 2	28 ± 3	24 ± 5	
<i>l</i> -PNC-24		48 ± 7	25 ± 3		

reported values.<sup>50</sup> Experiments characterizing the *l*-PNC particles were carried out in dilute aqueous suspensions, so these dimensions represent the polymer layer in a good solvent. This layer structure can then be contrasted with results for the pure *l*-PNC later in this section, in which the particle loading is much higher and Jeffamine M-2070 is the (theta) solvent.

DLS data for the bare silica and *l*-PNCs diluted in water are shown in Figure 1. The mean hydrodynamic diameters ( $D_h$ ) of  $15 \pm 2$  nm and  $24 \pm 2$  nm are equal within experimental error to both the diameters of 12.1–16.3 nm and 25.3–28.1 nm to the nominal particle size and a previous study of bare LUDOX HS and LUDOX TM particle sizes.<sup>50</sup> TEM images of dried samples, and SAXS of dilute aqueous suspensions, gave slightly larger average sizes (not shown).  $D_h$  increases from  $15 \pm 2$  nm to  $35 \pm 5$  nm for *l*-PNC-15 and  $24 \pm 2$  nm to  $48 \pm 7$  nm for *l*-PNC-24 following the grafting reaction, confirming that Jeffamine M-2070 was successfully attached to the particle surface. These size increases are consistent with previous studies.<sup>51</sup> The relative increase in  $D_h$  (20 nm for *l*-PNC-15 and 24 nm for *l*-PNC-24) is larger than the polymer radius of gyration ( $R_g = 3.2$  nm), which is expected because water is a good solvent for Jeffamine. In a good solvent, the grafted polymer swells and extends away from the particle surface in a brush conformation with a width much larger than  $R_g$ .<sup>52,53</sup> The absence of additional peaks in the DLS data suggests that particle aggregation is not responsible for the increase in  $D_h$ .

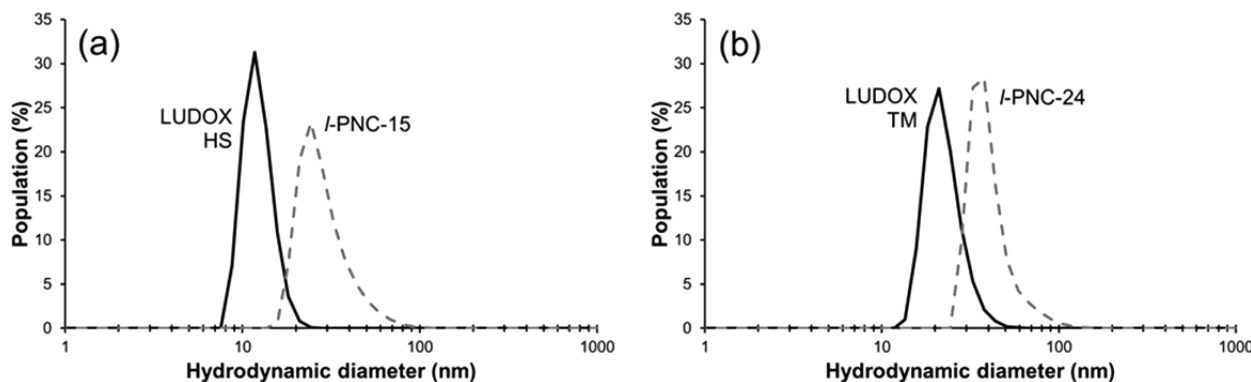


**Figure 1.** Hydrodynamic diameter distributions of (a) LUDOX HS silica particles (black solid line) and *l*-PNC-15 (gray dashed line) and (b) LUDOX TM silica particles (black solid line) and *l*-PNC-24 (gray dashed line).

Small-angle neutron scattering patterns of 10 wt % *s*-PNC-15 dispersed in H<sub>2</sub>O/D<sub>2</sub>O mixtures at three contrasts (Figure 2)

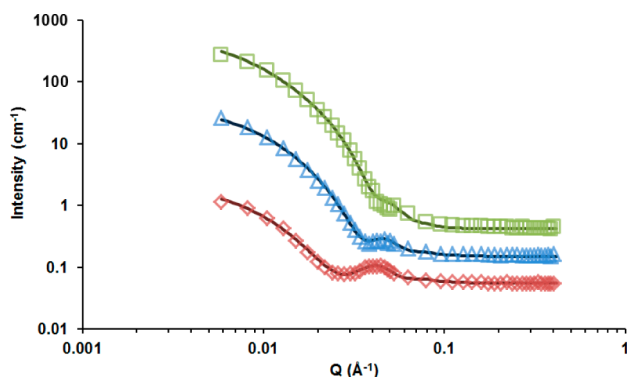


**Figure 2.** SANS patterns of *s*-PNC-15 particles dispersed in various H<sub>2</sub>O/D<sub>2</sub>O mixtures to give solvent scattering length densities of 3.0 (red diamonds), 4.0 (blue triangles), and 5.0 × 10<sup>-6</sup> Å<sup>-2</sup> (green squares), showing simultaneous fits to core + decaying-shell model.

show typical core–shell sphere scattering behavior, with the peak at ∼0.04 Å<sup>-1</sup> primarily arising from the hydrogenous polymer layer around the silica core. Neither homogeneous spheres nor a core + homogeneous shell model fit the data adequately, indicating that the polymer layer is not brush-like. Thus, a more complex model comprising polydisperse spheres with a shell with a radially varying scattering length density was employed.<sup>54</sup> This model consists of a homogeneous silica core, with a polymer coating whose scattering length density decreases linearly from a surface volume fraction to that of the solvent at its outermost, and is consistent with a mushroom-like or hemispherical polymer conformation, as expected for Jeffamine M-2070, a low molecular weight polymer in a theta solvent with a grafting density of ∼0.75 chains nm<sup>-2</sup>.<sup>20</sup>

The best-fit silica core diameter for the polymer-coated particles of 16.4 nm is in excellent agreement with the results from Table 1. The SANS best-fit shell thickness of 3.2 nm is smaller than expected based on the DLS data for *l*-PNC-15 in Figure 1. We attribute this to differences between the techniques. Whereas DLS measures the hydrodynamic polymer brush height, SANS is more sensitive to the polymer-rich component of the layer near the silica surface.<sup>55</sup> The higher particle concentration in the SANS sample compared to the DLS sample leads to compression of the polymer layer. In

addition, the particle concentration is much lower in DLS (0.1 wt %) compared to SANS (10 wt %). The SANS fitted volume fraction of polymer at the silica surface,  $\phi_p = 0.32$ , is consistent with the low grafting density determined from TGA on the dried product (without any free polymer remaining) of 0.7 chains nm<sup>-2</sup>. It is also consistent with a mushroom conformation, as it is below the expected threshold for a mushroom-to-brush transition (< 0.8 chains nm<sup>-2</sup>). The polymer layer thickness of 3.2 nm is somewhat larger than the hydrodynamic diameter of 2.2 ± 0.5 nm determined by DLS of Jeffamine M-2070 in water, which is to be expected for a freely draining coil. This indicates little chain extension of the polymer layer and is thus also consistent with a mushroom conformation. The grafted polymer layer structure on *s*-PNC-24 is expected to be very similar.

**Bulk and Interfacial Structure of *l*-PNCs.** Figure 3 shows the bulk nanostructure of pure, undiluted *l*-PNC-15 and *l*-PNC-

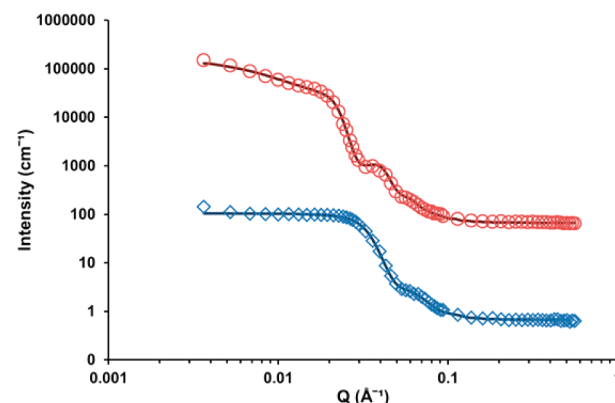


**Figure 3.** SANS patterns for *l*-PNC-15 (blue diamonds) and *l*-PNC-24 (red circles). Fits to the data are shown as solid black lines. The *l*-PNC-24 data is offset by 100× for clarity.

24 as revealed by SANS. Unlike in the aqueous PNC dispersions in which external contrast variation is achieved through H<sub>2</sub>O/D<sub>2</sub>O isotopic substitution, hydrogenous Jeffamine M-2070 serves as both the shell and host polymer in the *l*-PNCs. Thus, the scattering contrast is solely between the silica core and the (host + shell) polymer. As such, these experiments primarily probe the level of aggregation in the *l*-PNCs, which cannot be accessed using DLS because of multiple scattering due to the high particle volume fractions, as well as the high viscosity.

Scattering by *l*-PNC-15 is consistent with well-dispersed, slightly polydisperse spherical silica nanoparticles, but the upturn beginning at  $Q = 0.035 \text{ \AA}^{-1}$  in scattering in *l*-PNC-24 indicates the presence of clusters or aggregates.<sup>56</sup> The data was fit to a spherical form factor and hard sphere structure factor for *l*-PNC-15 and a square well structure factor for *l*-PNC-24 (see Table S2 in Supporting Information for fitting parameters). The square well structure factor was required to adequately fit the upturn at low  $Q$  for *l*-PNC-24. The fitted particle size, polydispersity, and volume fractions for *l*-PNC-15 and *l*-PNC-24 are presented in Table 2 and are in good agreement with other techniques used for the bare silica dispersions (c.f. Table 1).

**Table 2. Fitted Particle Diameter (nm), Polydispersity, and Volume Fraction of Bulk Liquid *l*-PNC-15 and *l*-PNC-24**

nanocomposite	particle diameter (nm)	polydispersity	volume fraction
<i>l</i> -PNC-15	16	0.21	0.18
<i>l</i> -PNC-24	28	0.16	0.15

The square well structure factor<sup>57</sup> models the low  $Q$  intensity increase in *l*-PNC-24 by introducing a narrow attractive potential well for each particle. The potential well is defined by the well depth ( $\varepsilon$  in units of  $kT$ ), which describes the magnitude of the interaction and whether it is repulsive or attractive, and the well width ( $\lambda$  in multiples of the particle diameter),<sup>57</sup> which is a measure of how far the potential extends from the particle center. For *l*-PNC-24, the fitted parameters are  $\varepsilon = 1.5 \text{ kT}$  and  $\lambda = 1.27$ , which indicates that the potential is weak, is attractive, and extends 35.5 nm from the particle center. This equates to 7.5 nm from the particle surface. The physical origin of interparticle attractions is most likely van der Waals forces. As the particles approach, free polymer is expelled but surface contact is prevented by the grafted polymer layers. Aggregation of the grafted polymer particles must be weak (meaning that clustering is reversible, consistent with the small  $\varepsilon$  value). When particle aggregation is irreversible, aggregates will grow over time and eventually sediment, leading to phase separation. Phase separation did not occur in these samples for at least 1 year. The SANS data for *l*-PNC-15 shows no evidence of objects larger than the silica particles. This is attributed to weaker van der Waals interactions in *l*-PNC-15, as this force scales with the particle size.

The average distance between particle centers, assuming the particles sit within the polymer matrix on a simple cubic lattice, for *l*-PNC-15 is 23 nm, which corresponds to an average surface separation of 7 nm between neighboring particle surfaces, and for *l*-PNC-24 is 43 nm, or 14 nm between neighboring particle surfaces. To a first approximation, as each surface has a grafted polymer layer  $\sim 3$  nm thick, this means that on average there is a free polymer film between the particles between 1 nm (*l*-PNC-15) and 8 nm (*l*-PNC-24) thick.

The structure of the air–*l*-PNCs interface was elucidated using tapping mode atomic force microscopy (TM-AFM) to probe the surface of *l*-PNC “droplets” on mica. The droplets were prepared according to a previous reported method.<sup>46</sup> In TM-AFM, the tip oscillates at or near its resonance frequency with a set amplitude. As the tip approaches the droplet, the amplitude of the driving oscillation is damped and the oscillating phase shifts. These changes are monitored via a feedback loop to generate topographic (height) and phase images.<sup>58</sup> The height images provide information on the *l*-PNC droplet dimensions, but the distribution of particles within the droplet is not visible (Figure S3 in Supporting Information). In contrast, the phase shift is sensitive to changes in compliance (hard or soft materials). Silica particles are visible as dark spots and polymers are visible as lighter colored areas in the phase images.<sup>46,59</sup> The distribution of polymer around the particles in *l*-PNCs is uniquely visualized; this information is not obtained in conventional TEM micrographs used in previous *l*-PNC studies.<sup>26,27,44</sup> Although Fernandes et al.<sup>19</sup> used high-angle annular dark field scanning transmission electron microscopy (HAADF STEM) to image the polymeric shell (10 kg/mol PEO-NH<sub>2</sub>) around a 16 nm silica nanoparticle, this does not show the distribution of polymer around multiple particles.

The TM-AFM phase images in Figure 4 show 2  $\mu\text{m} \times 2 \mu\text{m}$  scans of *l*-PNC-15 and *l*-PNC-24 with droplet heights of  $\sim 50$  nm (Figure S3 in Supporting Information). Within the droplets there are dark spots corresponding to hard silica particles at or near the droplet surface, separated by light regions of compliant host polymer.

Image analysis reveals that the average particle size is  $15 \pm 3$  and  $25 \pm 3$  nm for *l*-PNC-15 and *l*-PNC-24, respectively, consistent with results from DLS and SANS. In Figure 4a, a light-colored ring extends some distance from the droplet boundary. A similar feature was present for the droplet shown in Figure 4b, but the edge of the ring has been trimmed from the image at this scale. Jeffamine M-2070 has high affinity for

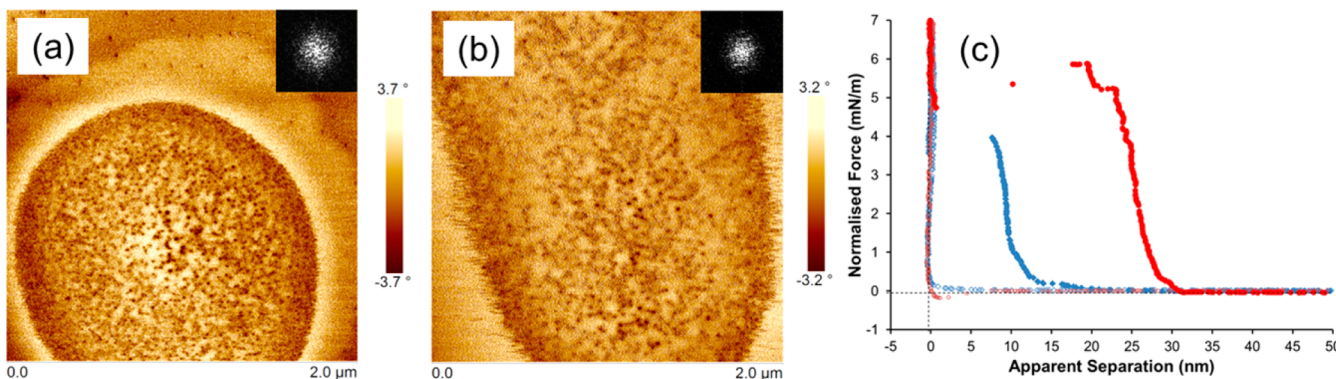


**Figure 4.** TM-AFM 2.0  $\mu\text{m}$  scan size phase images of (a) *l*-PNC-15 and (b) *l*-PNC-24 on mica. The insets show the 2D Fourier transform of the images. (c) Contact mode AFM normalized force versus separation curve of *l*-PNC-15 (blue diamonds) and *l*-PNC-24 (red circles) on mica with approach data as filled symbols and retraction data as open symbols.

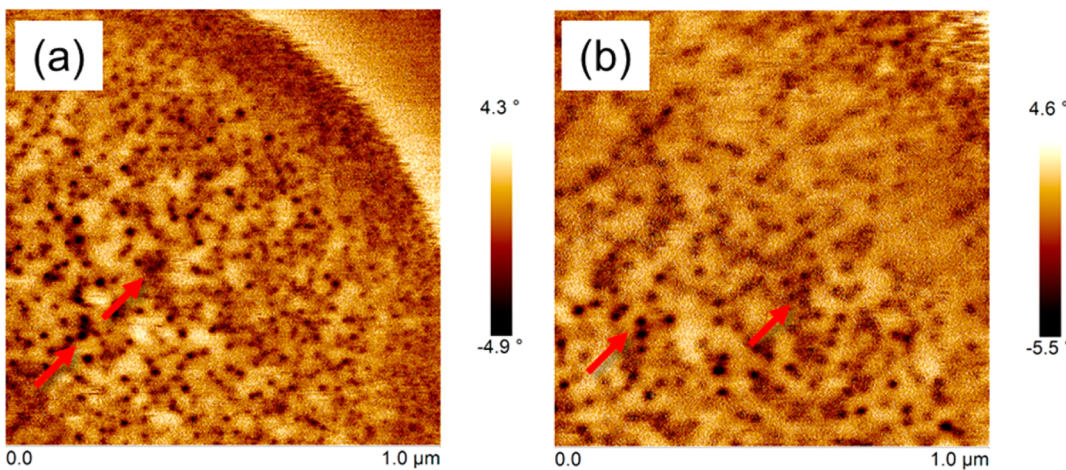


**Figure 5.** TM-AFM 1.0  $\mu\text{m}$  scan size phase images of (a) *l*-PNC-15 and (b) *l*-PNC-24 on mica. The red arrows point to areas with particle clustering.

the mica substrate (contact angle  $< 5^\circ$ ), so this light-colored ring is attributed to unbound Jeffamine M-2070 spreading across the mica surface. There are also areas on the surface of both droplets (but most obviously for *l*-PNC-24 in Figure 4b) that are polymer-rich. Successive AFM images show that the silica particles are mobile, consistent with a liquid state. In accordance with the SANS data, the TM-AFM images reveal that the particles are mostly well-dispersed in *l*-PNC-15, but there is significant clustering in *l*-PNC-24, which results in particle-rich and polymer-rich domains on the particle surface. The 2D Fourier transforms (FTs, insets in Figure 4) were added to provide an average spacing between dispersed particle centers in the AFM images. A 1  $\mu\text{m} \times 1 \mu\text{m}$  cropped image of the phase images in Figure 4 was used so that the FTs are not skewed by the droplet edges. The FTs show an intensity pattern that is brightest near the origin, then drops off in intensity. The distance from the origin to the end of the bright region of the FT (and inverted for real space) corresponds to the average repeat spacing of particle centers in the image. For *l*-PNC-15, the spacing is 27 nm, and for *l*-PNC-24, the spacing is 43 nm. These are broadly consistent with those determined from the SANS data (average distance between particle centers of 23 and 43 nm, respectively).

Contact mode AFM force curves were collected on the droplet surface (Figure 4c). This is the first reported study of the surface forces of *l*-PNCs. The force data collected over repeat experiments were remarkably similar. For both *l*-PNC-15 and *l*-PNC-24 no force was measured prior to the AFM tip making contact with the droplet surface. When the tip contacts the droplet surface, the force first rises gently, and then much more sharply, over a distance of  $\sim 10$  nm for *l*-PNC-15 and  $\sim 12$  nm for *l*-PNC-24. For *l*-PNC-15, when a force of 4 mN/m is reached the tip jumps  $\sim 10$  nm, and for *l*-PNC-24, when the force reaches 6 mN/m a jump  $\sim 20$  nm wide is seen. The form of the repulsive interaction is consistent with the grafted polymer layer between the tip and the silica surface, and on the underside of the particle and the droplet bulk, being compressed. Free polymer present in the compression zone will either diffuse away or collapse and thereby also contributes to the repulsion. The jump distance is larger for *l*-PNC-24 because of the larger silica particle size, and the push-through force is also higher because the volume of material that must be displaced to enable the jump is greater than that for *l*-PNC-15.

For both *l*-PNCs, the dimensions of the compressive region and the jump width are broadly consistent with the SANS data and the TM-AFM images. No adhesion was measured in either system upon retraction, indicating it is minimal because of the weak van der Waals interaction and the brush width being less than the entanglement length.<sup>60</sup>

From the force data, it is not possible to determine whether only one or a number of polymer-coated silica nanoparticles are displaced. Increasing the force up to the maximum possible with the cantilevers used did not further reduce the separation. As the AFM tip penetrates into the droplet following displacement of the first layer, the contact area between the tip and the *l*-PNC is increased. For the tip to penetrate further into the droplet, the second *l*-PNC layer beneath the tip apex and the first *l*-PNC layer in contact with the tip sides must both be displaced, which was not possible with the cantilevers used due to the high viscosity of the *l*-PNC.

Figure 5 shows 1  $\mu\text{m} \times 1 \mu\text{m}$  phase images of the *l*-PNCs, which highlight particle clustering. The higher resolution compared to Figure 4 allows particle clusters to be clearly identified (red arrows in Figure 5) as well as polymer-rich areas. In both images, the edge of the droplet is at the top right corner. For *l*-PNC-15, minor particle clustering is noted, but for *l*-PNC-24 significant clustering and a pronounced wide band of light-colored polymer (depleted of particles) is visible in the top half of the image. The distribution of particles is similar to previous TEM studies of NOHMs, except that the AFM can image the polymer in between particles.<sup>26,27,44</sup>

## CONCLUSIONS

Liquid polymer nanocomposites combine the functionality of hybrid materials with the processability of liquids and have the potential to be used in next-generation lubricants or carbon capture solvents. Stability of the nanoparticles is achieved by grafting polymer onto the particle surface and dispersing in a polymer melt. Depending on a wide number of factors, the *l*-PNC properties and phase stability can be tuned. However, the structure and distribution of particles within the bulk liquid and at a solid surface is relatively unexplored.

Two *l*-PNCs have been synthesized using 15 and 24 nm silica particles with  $\sim 30$  wt % silica content. Jeffamine M-2070 was covalently attached to the particle surfaces with grafting densities of 0.7–0.8 chains  $\text{nm}^{-2}$  on the 15 and 24 nm

particles and used as the host polymer. The PNC was a liquid when the polymer content was greater than ~30 wt %; lower polymer concentrations produced a solid material. Previously, these materials have been incorrectly characterized as C-NOHMs.

The combination of TM-AFM and SANS to reveal the interfacial and bulk structure of *l*-PNCs provides new information on stability in these systems. SANS revealed that the polymer-grafted particles were well-dispersed with minor clustering in *l*-PNC-15 but that more clusters were present in *l*-PNC-24. Similarly, TM-AFM images revealed significant clustering on the surface of *l*-PNC-24 droplets but minimal clustering on the surface of *l*-PNC-15. This is attributed to weaker van der Waals interactions between the smaller particles. Contact-mode AFM force curves revealed that a single layer of grafted-polymer particles could be displaced from under the tip with the cantilevers used. The spacing between silica particles on the surface of the droplet was consistent with the bulk measurements within error.

## ■ ASSOCIATED CONTENT

### Supporting Information

TGA curves of *l*-PNCs and *s*-PNCs, SANS fitting parameters, and TM-AFM height images. This material is available free of charge via the Internet at <http://pubs.acs.org>.

## ■ AUTHOR INFORMATION

### Corresponding Author

\*E-mail: rob.atkin@newcastle.edu.au.

### Notes

The authors declare no competing financial interest.

## ■ ACKNOWLEDGMENTS

This research was supported by an Australian Research Council Discovery Project (DP130102298). R.A. thanks the Australian Research Council Future Fellowship (FT120100313). The authors acknowledge Dave Phelan for his assistance with TEM experiments, Dr. Nirmesh Jain for his assistance with ultracentrifugation, Dr. Chris Garvey for his assistance with SANS experiments, and Dr. Zhengfei Chen for his assistance in data analysis. S.M. thanks the University of Newcastle for the provision of an Honours Scholarship.

## ■ REFERENCES

- (1) Kickelbick, G. Introduction to Hybrid Materials. In *Hybrid Materials: Synthesis, Characterization, and Applications*; Kickelbick, G., Ed.; John Wiley & Sons: Weinheim, Germany, 2007; pp 1–46.
- (2) Babu, S. S.; Nakanishi, T. Nonvolatile functional molecular liquids. *Chem. Commun.* **2013**, 49, 9373–9382.
- (3) Srivastava, S.; Schaefer, J. L.; Yang, Z.; Tu, Z.; Archer, L. A. 25th Anniversary Article: Polymer–Particle Composites: Phase Stability and Applications in Electrochemical Energy Storage. *Adv. Mater.* **2014**, 26, 201–234.
- (4) Kao, J.; Thorkelsson, K.; Bai, P.; Rancatore, B. J.; Xu, T. Toward functional nanocomposites: Taking the best of nanoparticles, polymers, and small molecules. *Chem. Soc. Rev.* **2013**, 42, 2654–2678.
- (5) Kickelbick, G.; Holzinger, D.; Brick, C.; Trimmel, G.; Moons, E. Hybrid Inorganic–Organic Core–Shell Nanoparticles from Surface-Functionalized Titanium, Zirconium, and Vanadium Oxo Clusters. *Chem. Mater.* **2002**, 14, 4382–4389.
- (6) Kumar, S. K.; Krishnamoorti, R. Nanocomposites: Structure, phase behavior, and properties. *Annu. Rev. Chem. Biomol. Eng.* **2010**, 1, 37–58.
- (7) Gomez-Romero, P.; Sanchez, C. Hybrid Materials, Functional Applications. An Introduction. In *Functional Hybrid Materials*; Gomez-Romero, P., Sanchez, C., Eds.; John Wiley & Sons: Weinheim, Germany, 2006; pp 1–14.
- (8) Sanchez, C.; Belleville, P.; Popall, M.; Nicole, L. Applications of advanced hybrid organic–inorganic nanomaterials: From laboratory to market. *Chem. Soc. Rev.* **2011**, 40, 696–753.
- (9) Fernandes, N. J.; Wallin, T. J.; Vaia, R. A.; Koerner, H.; Giannelis, E. P. Nanoscale Ionic Materials. *Chem. Mater.* **2014**, 26, 84–96.
- (10) Bourlinos, A. B.; Chowdhury, S. R.; Herrera, R.; Jiang, D. D.; Zhang, Q.; Archer, L. A.; Giannelis, E. P. Functionalised Nanostructures with Liquid-Like Behaviour: Expanding the Gallery of Available Nanostructures. *Adv. Funct. Mater.* **2005**, 15, 1285–1290.
- (11) Su, S.-J.; Kuramoto, N. Processable polyaniline–titanium dioxide nanocomposites: effect of titanium dioxide on the conductivity. *Synth. Met.* **2000**, 114, 147–153.
- (12) Leu, C.-M.; Chang, Y.-T.; Wei, K.-H. Polyimide-Side-Chain Tethered Polyhedral Oligomeric Silsesquioxane Nanocomposites for Low-Dielectric Film Applications. *Chem. Mater.* **2003**, 15, 3721–3727.
- (13) Warren, S. C.; Banholzer, M. J.; Slaughter, L. S.; Giannelis, E. P.; DiSalvo, F. J.; Wiesner, U. B. Generalized route to metal nanoparticles with liquid behavior. *J. Am. Chem. Soc.* **2006**, 128, 12074–12075.
- (14) Bourlinos, A. B.; Chowdhury, S. R.; Jiang, D. D.; An, Y.-U.; Zhang, Q.; Archer, L. A.; Giannelis, E. P. Layered Organosilicate Nanoparticles with Liquidlike Behaviour. *Small* **2005**, 1, 80–82.
- (15) Bourlinos, A. B.; Georgakilas, V.; Tzitzios, V.; Boukos, N.; Herrera, R.; Giannelis, E. P. Functionalized carbon nanotubes: synthesis of melttable and amphiphilic derivatives. *Small* **2006**, 2, 1188–1191.
- (16) Ramanathan, T.; Abdala, A. A.; Stankovich, S.; Dikin, D. A.; Herrera Alonso, M.; Piner, R. D.; Adamson, D. H.; Schniepp, H. C.; Chen, X.; Ruoff, R. S.; Nguyen, S. T.; Aksay, I. A.; Prud'Homme, R. K.; Brinson, L. C. Functionalized graphene sheets for polymer nanocomposites. *Nat. Nanotechnol.* **2008**, 3, 327–331.
- (17) Wu, L.; Zhang, B.; Lu, H.; Liu, C. Nanoscale ionic materials based on hydroxyl-functionalized graphene. *J. Mater. Chem. A* **2014**, 2, 1409–1417.
- (18) Zou, H.; Wu, S.; Shen, J. Polymer/silica nanocomposites: preparation, characterization, properties, and applications. *Chem. Rev.* **2008**, 108, 3893–3957.
- (19) Fernandes, N. J.; Akbarzadeh, J.; Peterlik, H.; Giannelis, E. P. Synthesis and Properties of Highly Dispersed Ionic Silica–Poly(ethylene oxide) Nanohybrids. *ACS Nano* **2013**, 7, 1265–1271.
- (20) Fernandes, N. J.; Koerner, H.; Giannelis, E. P.; Vaia, R. A. Hairy nanoparticle assemblies as one-component functional polymer nanocomposites: Opportunities and challenges. *MRS Commun.* **2013**, 3, 13–29.
- (21) Goyal, S.; Escobedo, F. A. Structure and transport properties of polymer grafted nanoparticles. *J. Chem. Phys.* **2011**, 135, 184902–184912.
- (22) Kim, J. H.; Kang, M.-S.; Kim, Y. J.; Won, J.; Park, N.-G.; Kang, Y. S. Dye-sensitized nanocrystalline solar cells based on composite polymer electrolytes containing fumed silica nanoparticles. *Chem. Commun.* **2004**, 1662–1663.
- (23) Kim, D.; Archer, L. A. Nanoscale Organic–Inorganic Hybrid Lubricants. *Langmuir* **2011**, 27, 3083–3094.
- (24) Lu, Y.; Moganty, S. S.; Korf, K.; Schaefer, J. L.; Das, S. K.; Archer, L. A.: Ionic Liquid-Nanoparticle Hybrid Electrolytes and Their Applications in Rechargeable Lithium Metal Batteries. In *Meeting Abstracts*; The Electrochemical Society: Pennington, NJ, 2013; pp 546–546.
- (25) Nugent, J. L.; Moganty, S. S.; Archer, L. A. Nanoscale Organic Hybrid Electrolytes. *Adv. Mater.* **2010**, 22, 3677–3680.
- (26) Schaefer, J. L.; Moganty, S. S.; Yanga, D. A.; Archer, L. A. Nanoporous hybrid electrolytes. *J. Mater. Chem.* **2011**, 21, 10094–10101.
- (27) Lin, K.-Y. A.; Park, A.-H. A. Effects of Bonding Types and Functional Groups on CO<sub>2</sub> Capture using Novel Multiphase Systems

- of Liquid-Like Nanoparticle Organic Hybrid Materials. *Environ. Sci. Technol.* **2011**, *45*, 6633–6639.
- (28) Lin, K. Y. A.; Petit, C.; Park, A.-H. A. Effect of SO<sub>2</sub> on CO<sub>2</sub> Capture Using Liquid-like Nanoparticle Organic Hybrid Materials. *Energy Fuels* **2013**, *27*, 4167–4174.
- (29) Park, Y.; Shin, D.; Jang, Y. N.; Park, A.-H. A. CO<sub>2</sub> Capture Capacity and Swelling Measurements of Liquid-like Nanoparticle Organic Hybrid Materials via Attenuated Total Reflectance Fourier Transform Infrared Spectroscopy. *J. Chem. Eng. Data* **2011**, *57*, 40–45.
- (30) Petit, C.; Bhatnagar, S.; Park, A.-H. A. Effect of water on the physical properties and carbon dioxide capture capacities of liquid-like Nanoparticle Organic Hybrid Materials and their corresponding polymers. *J. Colloid Interface Sci.* **2013**, *407*, 102–108.
- (31) Petit, C.; Park, Y.; Lin, K.-Y. A.; Park, A.-H. A. Spectroscopic Investigation of the Canopy Configurations in Nanoparticle Organic Hybrid Materials of Various Grafting Densities during CO<sub>2</sub> Capture. *J. Phys. Chem. C* **2012**, *116*, 516–525.
- (32) McEwan, M.; Green, D. Rheological impacts of particle softness on wetted polymer-grafted silica nanoparticles in polymer melts. *Soft Matter* **2009**, *5*, 1705–1716.
- (33) Srivastava, S.; Shin, J. H.; Archer, L. A. Structure and rheology of nanoparticle–polymer suspensions. *Soft Matter* **2012**, *8*, 4097–4108.
- (34) Sunday, D.; Ilavsky, J.; Green, D. L. A phase diagram for polymer-grafted nanoparticles in homopolymer matrices. *Macromolecules* **2012**, *45*, 4007–4011.
- (35) Bourlinos, A.; Chowdhury, S. R.; Jiang, D.; Zhang, Q. Weakly solvated PEG-functionalized silica nanoparticles with liquid-like behavior. *J. Mater. Sci.* **2005**, *40*, 5095–5097.
- (36) Jespersen, M. L.; Mirau, P. A.; von Meerwall, E. D.; Koerner, H.; Vaia, R. A.; Fernandes, N. J.; Giannelis, E. P. Hierarchical Canopy Dynamics of Electrolyte-Doped Nanoscale Ionic Materials. *Macromolecules* **2013**, *46*, 9669–9675.
- (37) Bourlinos, A.; Giannelis, E.; Zhang, Q.; Archer, L.; Floudas, G.; Fytas, G. Surface-functionalized nanoparticles with liquid-like behavior: The role of the constituent components. *Eur. Phys. J. E* **2006**, *20*, 109–117.
- (38) Bourlinos, A. B.; Herrera, R.; Chalkias, N.; Jiang, D. D.; Zhang, Q.; Archer, L.A.; Giannelis, E. P. Surface-Functionalised Nanoparticles with Liquid-Like Behaviour. *Adv. Mater.* **2005**, *17*, 234–237.
- (39) Chremos, A.; Panagiotopoulos, A. Z.; Yu, H.-Y.; Koch, D. L. Structure of solvent-free grafted nanoparticles: Molecular dynamics and density-functional theory. *J. Chem. Phys.* **2011**, *135*, 114901.
- (40) Jespersen, M. L.; Mirau, P. A.; Meerwall, E.; Vaia, R. A.; Rodriguez, R.; Giannelis, E. P. Canopy Dynamics in Nanoscale Ionic Materials. *ACS Nano* **2010**, *4*, 3735–3742.
- (41) Rodriguez, R.; Herrera, R.; Archer, L. A.; Giannelis, E. P. Nanoscale Ionic Materials. *Adv. Mater.* **2008**, *20*, 4353–4358.
- (42) Yu, H.-Y.; Koch, D. L. Predicting the Disorder–Order Transition of Solvent-Free Nanoparticle–Organic Hybrid Materials. *Langmuir* **2013**, *29*, 8197–8202.
- (43) Srivastava, S.; Agarwal, P.; Archer, L. A. Tethered Nanoparticle–Polymer Composites: Phase Stability and Curvature. *Langmuir* **2012**, *28*, 6276–6281.
- (44) Rodriguez, R.; Herrera, R.; Bourlinos, A. B.; Li, R.; Amassian, A.; Archer, L. A.; Giannelis, E. P. The synthesis and properties of nanoscale ionic materials. *Appl. Organomet. Chem.* **2010**, *24*, 581–589.
- (45) Hannecart, A.; Stanicki, D.; Vander Elst, L.; Muller, R. N.; Lecommandoux, S.; Thevenot, J.; Bonduelle, C.; Trotier, A.; Massot, P.; Miraux, S.; Sandre, O.; Laurent, S. Nano-thermometers with thermo-sensitive polymer grafted USPIOs behaving as positive contrast agents in low-field MRI. *Nanoscale* **2015**, *7*, 3754–3767.
- (46) Pyun, J.; Matyjaszewski, K.; Kowalewski, T.; Savin, D.; Patterson, G.; Kickelbick, G.; Huesing, N. Synthesis of well-defined block copolymers tethered to polysilsesquioxane nanoparticles and their nanoscale morphology on surfaces. *J. Am. Chem. Soc.* **2001**, *123*, 9445–9446.
- (47) Atkin, R.; Warr, G. G. Structure in confined room-temperature ionic liquids. *J. Phys. Chem. C* **2007**, *111*, 5162–5168.
- (48) Greenwood, P.; Gevert, B. Aqueous silane modified silica sols: theory and preparation. *Pigm. Resin Technol.* **2011**, *40*, 275–284.
- (49) Bel-Hassen, R.; Boufi, S.; Salon, M. C. B.; Abdelmouleh, M.; Belgacem, M. N. Adsorption of silane onto cellulose fibers. II. The effect of pH on silane hydrolysis, condensation, and adsorption behavior. *J. Appl. Polym. Sci.* **2008**, *108*, 1958–1968.
- (50) Goertz, V.; Dingenaerts, N.; Nirschl, H. Comparison of nanometric particle size distributions as determined by SAXS, TEM and analytical ultracentrifuge. *Part. Part. Syst. Charact.* **2009**, *26*, 17–24.
- (51) Barrera, C.; Herrera, A. P.; Bezires, N.; Fachini, E.; Olayo-Valles, R.; Hinestrosa, J. P.; Rinaldi, C. Effect of poly(ethylene oxide)-silane graft molecular weight on the colloidal properties of iron oxide nanoparticles for biomedical applications. *J. Colloid Interface Sci.* **2012**, *377*, 40–50.
- (52) Minko, S. Responsive polymer brushes. *J. Macromol. Sci., Polym. Rev.* **2006**, *46*, 397–420.
- (53) Dukes, D.; Li, Y.; Lewis, S.; Benicewicz, B.; Schadler, L.; Kumar, S. K. Conformational Transitions of Spherical Polymer Brushes: Synthesis, Characterization, and Theory. *Macromolecules* **2010**, *43*, 1564–1570.
- (54) Lonetti, B.; Tsikri, A.; Lang, P.; Stellbrink, J.; Willner, L.; Kohlbrecher, J.; Lettinga, M. Full Characterization of PB–PEO Wormlike Micelles at Varying Solvent Selectivity. *Macromolecules* **2011**, *44*, 3583–3593.
- (55) Linegar, K. L.; Adeniran, A. E.; Kostko, A. F.; Anisimov, M. A. Hydrodynamic radius of polyethylene glycol in solution obtained by dynamic light scattering. *Colloid J.* **2010**, *72*, 279–281.
- (56) El Harrak, A.; Carrot, G.; Oberdisse, J.; Jestin, J.; Boué, F. Atom transfer radical polymerization from silica nanoparticles using the ‘grafting from’ method and structural study via small-angle neutron scattering. *Polymer* **2005**, *46*, 1095–1104.
- (57) Sharma, R.; Sharma, K. The structure factor and the transport properties of dense fluids having molecules with square well potential, a possible generalization. *Phys. A* **1977**, *89*, 213–218.
- (58) García, R.; Pérez, R. Dynamic atomic force microscopy methods. *Surf. Sci. Rep.* **2002**, *47*, 197–301.
- (59) Qu, M.; Meth, J. S.; Blackman, G. S.; Cohen, G. M.; Sharp, K. G.; Van Vliet, K. J. Tailoring and probing particle–polymer interactions in PMMA/silica nanocomposites. *Soft Matter* **2011**, *7*, 8401–8408.
- (60) Watanabe, H. Viscoelasticity and dynamics of entangled polymers. *Prog. Polym. Sci.* **1999**, *24*, 1253–1403.